Coexistence of ferromagnetic and stripe antiferromagnetic spin fluctuations in $SrCo_2As_2$

Yu Li, Zhiping Yin, Zhonghao Liu, Weiyi Wang, Zhuang Xu, Yu Song, Long Tian, Yaobo Huang, Dawei Shen, D. L. Abernathy, J. L. Niedziela, R. A. Ewings, T. G. Perring, Daniel M. Pajerowski, Masaaki Matsuda, Philippe Bourges, Enderle Mechthild, Yixi Su, and Pengcheng Dai

Published version information

Citation: Y Li et al. "Coexistence of ferromagnetic and stripe antiferromagnetic spin fluctuations in $SrCo_2As_2$." Physical Review Letters, vol. 122, no. 11 (2019): 117204.

DOI: 10.1103/PhysRevLett.122.117204

Coexistence of Ferromagnetic and Stripe Antiferromagnetic Spin Fluctuations in $SrCo_2As_2$

Yu Li,[1,2] Zhiping Yin,[2,*] Zhonghao Liu,[3,†] Weiyi Wang,[1] Zhuang Xu,[2] Yu Song,[1] Long Tian,[2] Yaobo Huang,[4] Dawei Shen,[3] D. L. Abernathy,[5] J. L. Niedziela,[5] R. A. Ewings,[6] T. G. Perring,[6] Daniel M. Pajerowski,[5] Masaaki Matsuda,[5] Philippe Bourges,[7] Enderle Mechthild,[8] Yixi Su,[9] and Pengcheng Dai[1,2,‡]

[1]*Department of Physics and Astronomy, Rice University, Houston, Texas 77005, USA*
[2]*Department of Physics, Beijing Normal University, Beijing 100875, China*
[3]*State Key Laboratory of Functional Materials for Informatics and Center for Excellence in Superconducting Electronics, SIMIT, Chinese Academy of Sciences, Shanghai 200050, China*
[4]*Shanghai Synchrotron Radiation Facility, Shanghai Institute of Applied Physics, Chinese Academy of Sciences, Shanghai 201204, China*
[5]*Neutron Scattering Division, Oak Ridge National Laboratory, Oak Ridge, Tennessee 37831, USA*
[6]*ISIS Pulsed Neutron and Muon Source, STFC Rutherford Appleton Laboratory, Didcot, Oxfordshire, OX11 0QX, United Kingdom*
[7]*Laboratoire Léon Brillouin, CEA-CNRS, Université Paris-Saclay, CEA Saclay, 91191 Gif-sur-Yvette, France*
[8]*Institut Laue-Langevin, 6 rue Jules Horowitz, Boîte Postale 156, 38042 Grenoble Cedex 9, France*
[9]*Jülich Centre for Neutron Science (JCNS) at Heinz Maier-Leibnitz Zentrum (MLZ), Forschungszentrum Jülich, Lichtenbergstrasse 1, 85747 Garching, Germany*

(Received 8 August 2018; published 21 March 2019)

We use inelastic neutron scattering to study energy and wave vector dependence of spin fluctuations in $SrCo_2As_2$, derived from $SrFe_{2-x}Co_xAs_2$ iron pnictide superconductors. Our data reveal the coexistence of antiferromagnetic (AF) and ferromagnetic (FM) spin fluctuations at wave vectors $\mathbf{Q}_{AF} = (1, 0)$ and $\mathbf{Q}_{FM} = (0, 0)/(2, 0)$, respectively. By comparing neutron scattering results with those of dynamic mean field theory calculation and angle-resolved photoemission spectroscopy experiments, we conclude that both AF and FM spin fluctuations in $SrCo_2As_2$ are closely associated with a flatband of the e_g orbitals near the Fermi level, different from the t_{2g} orbitals in superconducting $SrFe_{2-x}Co_xAs_2$. Therefore, Co substitution in $SrFe_{2-x}Co_xAs_2$ induces a t_{2g} to e_g orbital switching, and is responsible for FM spin fluctuations detrimental to the singlet pairing superconductivity.

DOI: 10.1103/PhysRevLett.122.117204

Flat electronic bands can give rise to a plethora of interaction-driven quantum phases, including ferromagnetism [1], a Mott insulating phase due to electron correlations [2], and superconductivity [3]. Therefore, an understanding of how the flat electronic bands can influence the electronic, magnetic, and superconducting properties of solids is an important topic in condensed matter physics. In iron pnictide superconductors such as $AFe_{2-x}Co_xAs_2$ (A = Ba, Sr) [Figs. 1(a)–1(d)], the dominant interactions are stripe antiferromagnetic (AF) order, and superconductivity, which has singlet electron pairing, arises by doping an electron with Co substitution to suppress static AF order [4–6]. While AF spin fluctuations and superconductivity in iron pnictides are believed to arise from nested hole Fermi surfaces at Γ and electron Fermi surfaces at M [Fig. 1(e)] [7], the density functional theory (DFT) calculations suggest competing ferromagnetic (FM) and AF spin fluctuations with the balance controlled by doping [8,9]. For Co-overdoped ACo_2As_2 [10,11], where the DFT calculations find a tendency for both the FM and AF order, neutron scattering revealed only the AF spin fluctuations [12] while angle-resolved photoemission spectroscopy (ARPES) experiments found no evidence of the Fermi surface nesting [13,14]. On the other hand, nuclear magnetic resonance (NMR) measurements on $AFe_{2-x}Co_xAs_2$ provided evidence for FM spin fluctuations at all Co-doping levels in addition to the AF spin fluctuations [15,16]. In particular, strong FM spin fluctuations in $AFe_{2-x}Co_xAs_2$ are believed to compete with AF spin fluctuations and prevent superconductivity for Co-overdoped samples [15,16], contrary to the Fermi surface nesting picture where superconductivity is suppressed via vanishing hole Fermi surfaces with increasing Co doping [7,17]. Finally, action of physical, chemical pressure, or aliovalent substitution in BCo_2As_2 (B = Eu, Ca) can drive these AF materials into ferromagnets [18]. In particular, $CaCo_{1.84}As_2$ with a collapsed tetragonal structure [19] forms an A-type AF ground state with coexisting FM spin fluctuations within the CoAs layer and A-type AF spin fluctuations between the CoAs layers [20]. These features are different from those of $Ca(Fe_{1-x}Co_x)_2As_2$ [21,22] and $AFe_{2-x}Co_xAs_2$ [6].

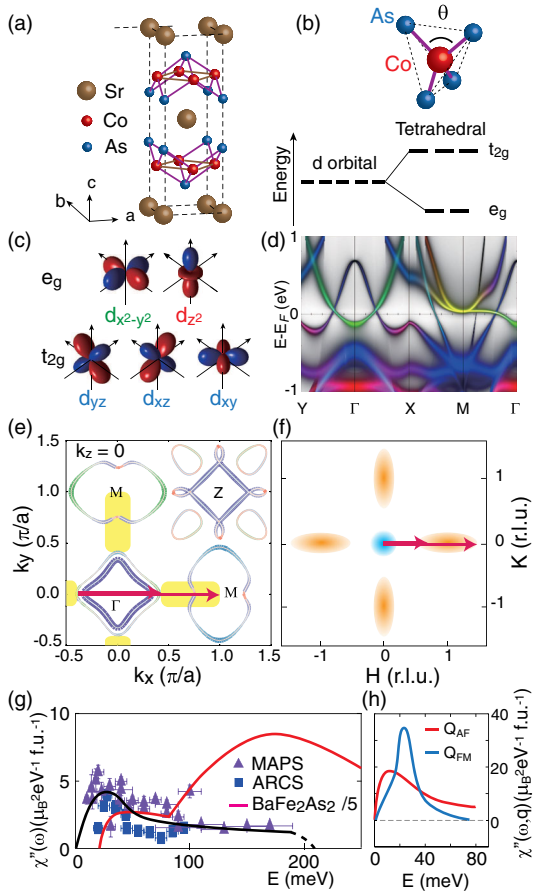

FIG. 1. (a) Crystal structure of $SrCo_2As_2$. (b) The tetrahedron of Fe(Co)As_4 and the resulting d-orbital splitting. (c) Wave functions of the five d orbitals. (d) Band structure of $SrCo_2As_2$. Green (red) represents the $d_{x^2-y^2}(d_{z^2})$ orbital and blue is the contribution from the t_{2g} (d_{xz}, d_{yz}, d_{xy}) orbitals. Yellow is the mixture of red (d_{z^2}) and green ($d_{x^2-y^2}$). (e) Fermi surfaces from DFT + DMFT calculations. The shading yellow area corresponds to the flatband (yellow part) in Fig. 1(d) and arrows represent scattering wave vectors associated with the flatband. The colors represent the same orbital characters as in (c) and (d). (f) Schematics of the low energy FM (blue) and AF (orange) spin fluctuations in $SrCo_2As_2$. (g) Energy dependence of integrated $\chi''(E)$ of $SrCo_2As_2$ in absolute units normalized by using a vanadium standard [23]. The red solid line is $\chi''(E)/5$ of $BaFe_2As_2$ [28]. The black solid line is a guide to the eye. (h) The measured AF and FM fluctuations at $\mathbf{Q}_{AF}$ and $\mathbf{Q}_{FM}$ [23].

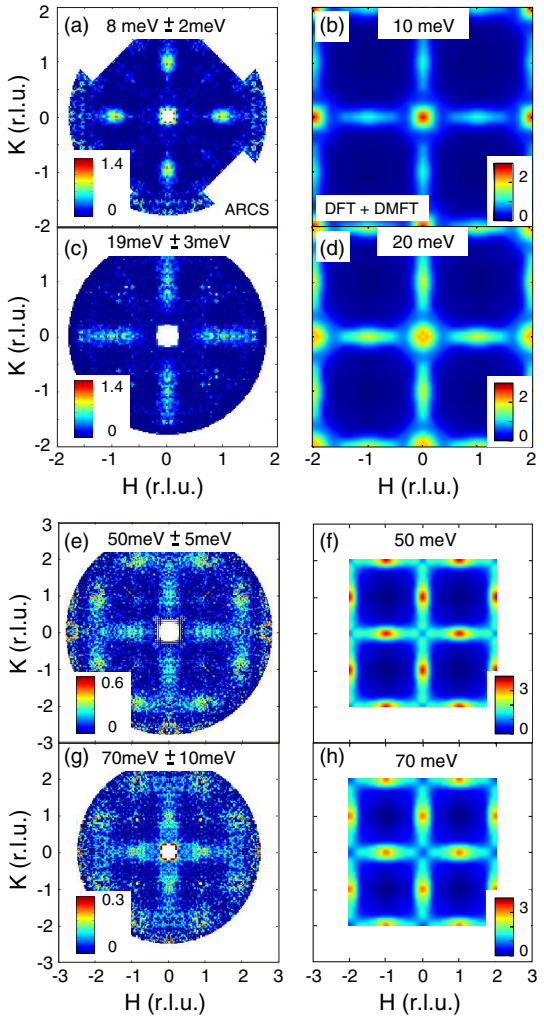

FIG. 2. (a),(c),(e),(g) Two-dimensional images of measured dynamic spin susceptibility of $SrCo_2As_2$ in the $[H, K]$ plane at $E = 8 \pm 2$, 19 ± 3, 50 ± 5, and 70 ± 10 meV, respectively. Radially symmetric backgrounds were subtracted to visually enhance the weak magnetic signal. (b),(d),(f),(h) The corresponding results from the DFT + DMFT calculations [23].

Iron pnictides have five nearly degenerate d orbitals which split into t_{2g} and e_g orbitals in a tetrahedral crystal field [Figs. 1(b) and 1(c)]. The electronic structure of the system is dominated by Fe $3d$ t_{2g} orbitals near the Fermi level with hole-electron Fermi surfaces at Γ and M, respectively [Fig. 1(e)]. The presence of multiple Fe $3d$ orbitals near the Fermi level results in varying orbital characters on different parts of the Fermi surfaces [29], and orbital-dependent strengths of electronic correlations [30–34]. The electronic band structures of $SrCo_2As_2$ calculated by DFT combined with dynamic mean field theory (DMFT) [35,36] reveal the presence of a flatband near the M point with a mixture of the d_{z^2} and $d_{x^2-y^2}$ orbitals [Fig. 1(d)]. If $SrCo_2As_2$ has a strong ferromagnetism arising from the flatband as suggested from NMR [15,16], one should be able to extract its energy and wave vector dependence by neutron scattering and determine its role to the suppressed superconductivity in Co-overdoped $SrFe_{2-x}Co_xAs_2$ [4–6].

In this Letter, we combine neutron scattering, ARPES, and DFT + DMFT methods to study $SrCo_2As_2$, an electron-doped end member of $SrFe_{2-x}Co_xAs_2$ exhibiting no structural, magnetic, or superconducting transitions [11]. Besides confirming the longitudinally elongated AF spin fluctuations at wave vector $\mathbf{Q}_{AF} = (1, 0)$ [Figs. 1(f) and 2] [12], we successfully observed the in-plane FM spin fluctuations at $\mathbf{Q}_{FM} = (0, 0)$ and its equivalent (2,0)

positions [Figs. 2 and 3]. From the DFT + DMFT calculations and ARPES measurements, we find a flatband consisting of the e_g orbitals along the Γ-M direction right above the Fermi level [Fig. 1(d)], leading to a prominent peak in the density-of-state (DOS) near Fermi level responsible for both the FM and AF spin fluctuations [Figs. 4(a)–4(d)]. Orbital analysis of the dynamic spin susceptibility $\chi''(\mathbf{Q}, E)$ in the DFT + DMFT calculations suggests that magnetism in $SrCo_2As_2$ is dominated by the e_g orbitals [Figs. 1(d), 1(e), 4(e), 4(f)]. These results are beyond the prevailing orbital selective Mott picture in iron pnictides, where the t_{2g} orbitals are most strongly correlated [29,33,37–39] and electron (Co) doping monotonically reduces correlations in all five d orbitals [30,31]. In addition, the FM spin correlations in $SrCo_2As_2$ are similar to the A-type AF order in $CaCo_{1.86}As_2$ [40]. Therefore, our observation is consistent with the proposal that FM fluctuations are detrimental to superconductivity in Co-overdoped $AFe_{2-x}Co_xAs_2$ and may be responsible for the hole-electron asymmetry of the superconducting dome in iron pnictide families [16].

We begin by showing constant-energy slices of $\chi''(\mathbf{Q}, E)$ on $SrCo_2As_2$ at $T = 5$ K [Figs. 2(a), 2(c), 2(e), 2(g)] [23,38]. At $E = 8$ meV, the AF spin fluctuations at $\mathbf{Q}_{AF} = (1, 0)$ are longitudinally elongated similar to that in hole-doped $BaFe_2As_2$ [Fig. 2(a)] [17]. With increasing energy, spin fluctuations along the longitudinal direction are further elongated while they barely change along the transverse direction, different from the transversely elongated spin fluctuations in $AFe_{2-x}Co_xAs_2$ [6,17]. At $E \geq 50$ meV, there are magnetic intensities at both the $\mathbf{Q}_{AF} = (1, 0)$ and $\mathbf{Q}_{FM} = (2, 0)$. Spin fluctuations form ridges of scattering across the whole Brillouin zone forming a square network [Figs. 2(e), 2(g)], similar to those in $CaCo_{2-y}As_2$ [20]. Along the transverse direction, we observed a linearly broadening of the half-width at half-maximum (HWHM) of AF spin fluctuations with increasing energy at the speed of $\Delta\text{HWHM}/\Delta E \approx 1/(440\ \text{meV Å})$ [23] and no peak splitting was identified.

We used DFT + DMFT calculations to understand the electronic band structure [Fig. 1(d)] and spin dynamics of $SrCo_2As_2$ [23,30,41]. Figures 2(b), 2(d), 2(f), and 2(h) show the DFT + DMFT calculated results for $E = 10$, 20, 50, 70 meV. Although the calculated results look remarkably similar to experimental data in Figs. 2(a), 2(c), 2(e), and 2(g), there are also important differences. First, the AF spin fluctuations are weaker than the FM spin fluctuations in the DFT + DMFT calculation at $E = 10$ meV, while they are stronger in experiments. This is mostly because the calculations are exceedingly sensitive to the position of the flatband with respect to the Fermi level. Second, the calculation suggests that FM spin fluctuations originating from the Γ (and equivalent) point merge into AF spin fluctuations at $\mathbf{Q}_{AF} = (\pm 1, 0)/(0, \pm 1)$ around 50 meV [Fig. 2(f)], while there is no clear evidence of FM spin fluctuations at $E = 8$, 19 meV [Figs. 2(a), 2(c)] [23]. Figure 1(g) shows energy dependence of local dynamic susceptibility $\chi''(E)$, obtained by integrating both the FM and AF signal within the area of $(0, 0) \rightarrow (1, 1) \rightarrow (2, 0) \rightarrow (1, -1) \rightarrow (0, 0)$ [6], and its comparison with those of $BaFe_2As_2$ [28]. The total fluctuating moment is approximately $\langle m^2 \rangle \approx 0.4 \pm 0.1\ \mu_B^2/\text{f.u.}$ [23,28], compared with $0.5\ \mu_B^2/\text{f.u.}$ from the calculation. Because of the diffusive nature of the magnetic scattering (Signal or SIG), it is rather difficult to experimentally separate the integrated FM and AF signal and compare with that of the DFT + DMFT calculations.

To conclusively determine the FM signal in $SrCo_2As_2$, we carried out polarized neutron scattering experiments with the neutron polarization directions x, y, and z shown in Fig. 3(a), which correspond to neutron spin-flip (SF) scattering cross sections σ_x^{SF}, σ_y^{SF}, and σ_z^{SF}, respectively [42–47]. The magnetic scattering of $SrCo_2As_2$ should then be $\text{SIG} = \sigma_x^{SF} - (\sigma_y^{SF} + \sigma_z^{SF})/2$ [43–47]. Figures 3(c) and 3(d) show the energy scans at $\mathbf{Q}_1 = (1, 0, 1)$ and $\mathbf{Q}_2 = (0, 0, 3)$ [Fig. 3(a)]. Figure 3(e) shows energy dependence of SIG at $\mathbf{Q}_1$ and $\mathbf{Q}_2$, confirming the presence of magnetic fluctuations at the AF and FM wave vectors, respectively.

At $\mathbf{Q}_1$ [Fig. 3(c)], $\sigma_y^{SF} \approx \sigma_z^{SF}$ implies that the AF spin fluctuations are isotropic in spin space, different from the anisotropic spin fluctuations in $BaFe_{2-x}Co_xAs_2$ induced by spin-orbit coupling [43–47]. These results suggest that the spin-orbit coupling in $SrCo_2As_2$ is weaker than that of $BaFe_2As_2$. At $\mathbf{Q}_2$ [Figs. 3(d), 3(e)], magnetic scattering increases with increasing energy with no spin gap above $E = 3$ meV, providing direct evidence for the FM spin fluctuations in $SrCo_2As_2$ [15,23]. To further demonstrate the coexisting FM and AF spin fluctuations, we performed constant-energy scans along the $[H, 0, 3]$ and $[H, 0, 1]$ directions at $E = 8$ meV [Fig. 3(b)]. Figure 3(f) indicates that the FM spin fluctuations are confined near (0,0,3) and are about half the size of that of the AF signal around (1,0,1). The DFT + DMFT calculations predict the dominant FM spin fluctuations around 10 meV [Fig. 2(b)]. Constant-energy scans along the $[1, 0, L]$ [Fig. 3(g)] and $[0, 0, L]$ [Fig. 3(h)] directions reveal weakly L dependent scattering at both the AF and FM positions, respectively, confirming the quasi-two-dimensional nature of the magnetic scattering. Figure 1(h) shows energy dependence of $\chi''(\mathbf{Q}, E)$ at $\mathbf{Q}_{AF}$ and $\mathbf{Q}_{FM}$, where the peak in $\mathbf{Q}_{FM}$ near 25 meV should be associated with the Van Hove singularity of the flatband.

To understand the origin of the FM and AF spin fluctuations in $SrCo_2As_2$ [Fig. 4(a)], we measured its band structure by ARPES and compared the outcome in Fig. 4(c) with the DFT + DMFT calculations in Fig. 4(d). Around the Γ point, one shallow electronlike α band and one highly dispersive holelike β band were observed. Another electronlike band at the M point was also found. These results agree well with the DFT + DMFT calculation in Fig. 4(d), supporting the existence of a flatband along the Γ-M

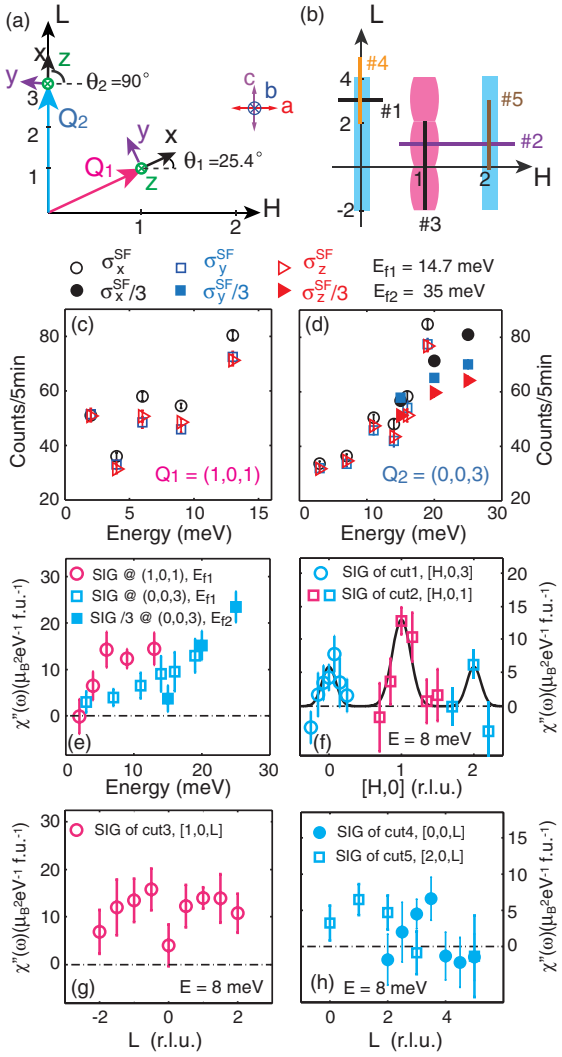

FIG. 3. (a) Schematic of the $[H, 0, L]$ scattering plane for neutron polarization analysis. The AF and FM wave vectors are labeled as $\mathbf{Q}_1$ and $\mathbf{Q}_2$, respectively. The neutron polarization directions are along the x, y, and z. (b) Locations of FM (blue) and AF (magenta) spin fluctuations in reciprocal space. Lines indicate scan directions. (c),(d) Constant-$\mathbf{Q}$ scans of σ_x^{SF}, σ_y^{SF}, and σ_z^{SF} at $\mathbf{Q}_1$ and $\mathbf{Q}_2$, respectively, at $T = 1.5$ K. (e) Constant-Q scans of pure magnetic scattering intensity at $\mathbf{Q}_1$ and $\mathbf{Q}_2$. (f),(g),(h) The AF (magenta) and FM (blue) scattering at $E = 8$ meV along the H and L directions as marked in (b). The values of SIG are converted into absolute units by assuming the polarized data at $\mathbf{Q}_{\mathrm{AF}} = (1, 0, 1)$ and $E = 8$ meV are comparable with the integrated intensity in $0.975 < \mathrm{H} < 1.025$ and $-0.1 < \mathrm{K} < 0.1$ in Fig. 2(a).

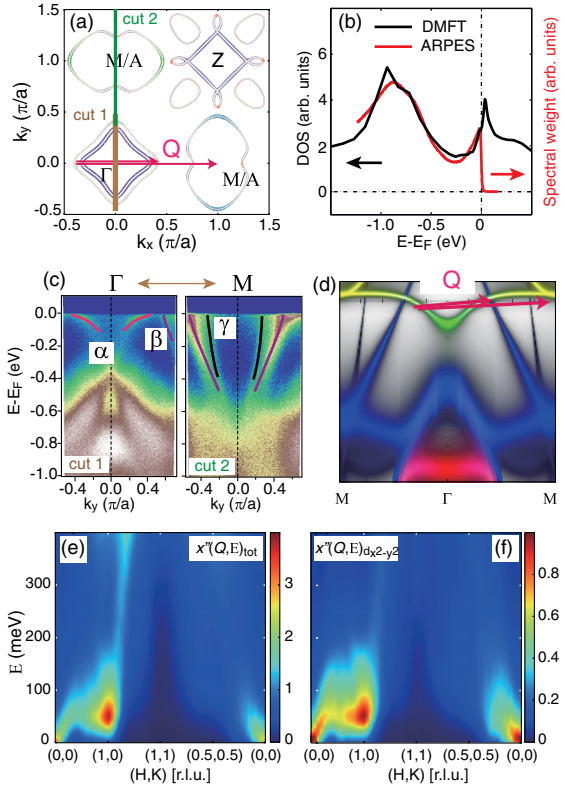

FIG. 4. (a) Fermi surfaces of $SrCo_2As_2$ from the DFT + DMFT calculations. (b) Calculated electronic DOS and integrated spectral weight from ARPES. (c) Intensity plots of the band dispersion along the Γ-M direction ($E_{\mathrm{photon}} = 22$ eV). (d) Calculated band structure along the M-Γ-M direction. Arrows indicate possible wave vectors from occupied to empty states on the flatband. (e) Total $\chi''(\mathbf{Q}, E)$ from the DFT + DMFT calculation. (f) Calculated $\chi''(\mathbf{Q}, E)$ from the $d_{x^2-y^2}$ orbital.

direction right above the Fermi level [Figs. 1(d) and 4(d)] [23]. Further ARPES data collected along the Z-A direction with a different photon energy reveals the presence of the flatband (or band bottom) touching the Fermi level at the A point, mainly arising from the $d_{x^2-y^2}$ orbital hybridized with the d_{z^2} [Fig. 1(d)] [23]. In particular, the partial DOS of the Co $3d_{x^2-y^2}$ orbital in the DFT + DMFT calculation exhibits a peak at about 35 meV above the Fermi level, similar to the maximum scattering of the FM spin fluctuations [Fig. 1(h)], suggesting a close relationship between the flatband and FM instability.

Flat electronic bands with high DOS near the Fermi level can influence the electronic and magnetic properties of solids through tuning the electron-electron correlations [1–3]. In $SrCo_2As_2$, the flatband might affect spin fluctuations in two ways. First, the $d_{x^2-y^2}$ band (α) dispersive along the Γ-X/Y direction but flat along the Γ-M direction [Fig. 1(d)] might lead to high DOS near the Fermi level and Stoner FM instability similar to that of Sr_2RuO_4 [48,49]. Both the DFT + DMFT calculations and ARPES experiments reveal a prominent peak in DOS near the Fermi level [Fig. 4(b)], supporting the existence of flatband related FM fluctuations. Second, the flatband above the Fermi level provides many electron scattering channels as shown by the arrows in Fig. 4(d). These scattering processes result in the longitudinally elongated spin fluctuations extending from Γ to M [Fig. 1(f)]. This is different from the longitudinally elongated low-energy spin fluctuations in

hole-doped $BaFe_2As_2$, where the longitudinal elongation is driven by mismatched sizes of the hole-electron Fermi surfaces [17,50–52]. Figures 4(e) and 4(f) plot the DFT + DMFT calculated total dynamic spin susceptibility and contributions from the $d_{x^2-y^2}$ orbital [23]. Surprisingly, both the AF and FM spin fluctuations are dominated by the e_g orbitals (Fig. S5) [23], different from the majority t_{2g} contributions to the spin dynamics in iron pnictides [41]. In $SrFe_{2-x}Co_xAs_2$, the presence of AF spin fluctuations [12] is responsible for the superconductivity. The appearance of FM spin fluctuations in $SrCo_2As_2$ and their competition with the stripe AF spin fluctuations might be responsible the absence of superconductivity in heavily overdoped $SrFe_{2-x}Co_xAs_2$. The underlying orbital characters might also be an important factor for superconductivity in iron pnictides.

The work at Rice is supported by the U.S. NSF DMR-1700081 and the Robert A. Welch Foundation Grant No. C-1839 (P. D.). Z. P. Y. was supported by the NSFC (Grant No. 11674030), the Fundamental Research Funds for the Central Universities (Grant No. 310421113), the National Key Research and Development Program of China Grant No. 2016YFA0302300. The calculations used high performance computing clusters at BNU in Zhuhai and the National Supercomputer Center in Guangzhou. Z. H. L. acknowledges the NSFC (Grant No. 11704394), and the Shanghai Sailing Program (Grant No. 17YF1422900). This research used resources at the High Flux Isotope Reactor and Spallation Neutron Source, a DOE Office of Science User Facility operated by the Oak Ridge National Laboratory. Experiments at the ISIS Neutron and Muon Source were supported by a beam time allocation RB1610397 from the Science and Technology Facilities Council.

*yinzhiping@bnu.edu.cn
†lzh17@mail.sim.ac.cn
‡pdai@rice.edu

[1] H. Tasaki, Prog. Theor. Phys. **99**, 489 (1998).
[2] Y. Cao, V. Fatemi, A. Demir, S. Fang, S. L. Tomarken, J. Y. Luo, J. D. Sanchez-Yamagishi, K. Watanabe, T. Taniguchi, E. Kaxiras, R. C. Ashoori, and P. Jarillo- Herrero, Nature (London) **556**, 80 (2018).
[3] Y. Cao, V. Fatemi, S. Fang, K. Watanabe, T. Taniguchi, E. Kaxiras, and P. Jarillo-Herrero, Nature (London) **556**, 43 (2018).
[4] D. C. Johnston, Adv. Phys. **59**, 803 (2010).
[5] D. J. Scalapino, Rev. Mod. Phys. **84**, 1383 (2012).
[6] P. C. Dai, Rev. Mod. Phys. **87**, 855 (2015).
[7] P. J. Hirschfeld, M. M. Korshunov, and I. I. Mazin, Rep. Prog. Phys. **74**, 124508 (2011).
[8] D. J. Singh and M.-H. Du, Phys. Rev. Lett. **100**, 237003 (2008).
[9] I. I. Mazin, D. J. Singh, M. D. Johannes, and M. H. Du, Phys. Rev. Lett. **101**, 057003 (2008).
[10] A. S. Sefat, D. J. Singh, R. Jin, M. A. McGuire, B. C. Sales, and D. Mandrus, Phys. Rev. B **79**, 024512 (2009).
[11] A. Pandey, D. G. Quirinale, W. Jayasekara, A. Sapkota, M. G. Kim, R. S. Dhaka, Y. Lee, T. W. Heitmann, P. W. Stephens, V. Ogloblichev, A. Kreyssig, R. J. McQueeney, A. I. Goldman, A. Kaminski, B. N. Harmon, Y. Furukawa, and D. C. Johnston, Phys. Rev. B **88**, 014526 (2013).
[12] W. Jayasekara, Y. Lee, A. Pandey, G. S. Tucker, A. Sapkota, J. Lamsal, S. Calder, D. L. Abernathy, J. L. Niedziela, B. N. Harmon, A. Kreyssig, D. Vaknin, D. C. Johnston, A. I. Goldman, and R. J. McQueeney, Phys. Rev. Lett. **111**, 157001 (2013).
[13] N. Xu, P. Richard, A. van Roekeghem, P. Zhang, H. Miao, W. L. Zhang, T. Qian, M. Ferrero, A. S. Sefat, S. Biermann, and H. Ding, Phys. Rev. X **3**, 011006 (2013).
[14] R. S. Dhaka, Y. Lee, V. K. Anand, D. C. Johnston, B. N. Harmon, and A. Kaminski, Phys. Rev. B **87**, 214516 (2013).
[15] P. Wiecki, V. Ogloblichev, A. Pandey, D. C. Johnston, and Y. Furukawa, Phys. Rev. B **91**, 220406(R) (2015).
[16] R. Wiecki, B. Roy, D. C. Johnston, S. L. Bud'ko, P. C. Canfield, and Y. Furukawa, Phys. Rev. Lett. **115**, 137001 (2015).
[17] M. Wang, C. Zhang, X. Lu, G. Tan, H. Luo, Y. Song, M. Wang, X. Zhang, E. A. Goremychkin, T. G. Perring, T. A. Maier, Z. Yin, K. Haule, G. Kotliar, and P. C. Dai, Nat. Commun. **4**, 2874 (2013).
[18] X. Tan, G. Fabbris, D. Haskel, A. A. Yaroslavtsev, H. Cao, C. M. Thompson, K. Kovnir, A. P. Menushenkov, R. V. Chernikov, V. O. Garlea, and M. Shatruk, J. Am. Chem. Soc. **138**, 2724 (2016).
[19] A. Kreyssig, M. A. Green, Y. Lee, G. D. Samolyuk, P. Zajdel, J. W. Lynn, S. L. Bud'ko, M. S. Torikachvili, N. Ni, S. Nandi, J. B. Leão, S. J. Poulton, D. N. Argyriou, B. N. Harmon, R. J. McQueeney, P. C. Canfield, and A. I. Goldman, Phys. Rev. B **78**, 184517 (2008).
[20] A. Sapkota, B. G. Ueland, V. K. Anand, N. S. Sangeetha, D. L. Abernathy, M. B. Stone, J. L. Niedziela, D. C. Johnston, A. Kreyssig, A. I. Goldman, and R. J. McQueeney, Phys. Rev. Lett. **119**, 147201 (2017).
[21] A. Sapkota, P. Das, A. E. Böhmer, B. G. Ueland, D. L. Abernathy, S. L. Bud'ko, P. C. Canfield, A. Kreyssig, A. I. Goldman, and R. J. McQueeney, Phys. Rev. B **97**, 174519 (2018).
[22] J. Zhao, D. T. Adroja, D.-X. Yao, R. Bewley, S. Li, X. F. Wang, G. Wu, X. H. Chen, J. Hu, and P. C. Dai, Nat. Phys. **5**, 555 (2009).
[23] See Supplemental Material at http://link.aps.org/supplemental/10.1103/PhysRevLett.122.117204 for details of experimental setup and theoretical calculation, which include Refs. [4,11,23–27,30,35,36].
[24] P. Blaha, K. Schwarz, G. Madsen, D. Kvasnicka, and J. Luitz, *WIEN2K, An Augmented Plane Wave+Local Orbitals Program for Calculating Crystal Properties* (Karlheinz Schwarz, Technische Universität Wien, Austria, 2001).
[25] Z. P. Yin, K. Haule, and G. Kotliar, Nat. Phys. **7**, 294 (2011).
[26] K. Haule, Phys. Rev. B **75**, 155113 (2007).
[27] P. Werner, A. Comanac, L. de' Medici, M. Troyer, and A. J. Millis, Phys. Rev. Lett. **97**, 076405 (2006).
[28] L. W. Harriger, H. Q. Luo, M. S. Liu, C. Frost, J. P. Hu, M. R. Norman, and P. C. Dai, Phys. Rev. B **84**, 054544 (2011).

[29] M. Yi, Y. Zhang, Z.-X. Shen, and D. Lu, npj Quantum Mater. **2**, 57 (2017).
[30] Z. P. Yin, K. Haule, and G. Kotliar, Nat. Mater. **10**, 932 (2011).
[31] L. de' Medici, G. Giovannetti, and M. Capone, Phys. Rev. Lett. **112**, 177001 (2014).
[32] E. M. Nica, R. Yu, and Q. Si, npj Quantum Mater. **2**, 24 (2017).
[33] Q. Si, R. Yu, and E. Abrahams, Nat. Rev. Mater. **1**, 16017 (2016).
[34] Z.-H. Liu, A. N. Yaresko, Y. Li, D. V. Evtushinsky, P.-C. Dai, and S. V. Borisenko, Appl. Phys. Lett. **112**, 232602 (2018).
[35] G. Kotliar, S. Y. Savrasov, K. Haule, V. S. Oudovenko, O. Parcollet, and C. A. Marianetti, Rev. Mod. Phys. **78**, 865 (2006).
[36] K. Haule, C.-H. Yee, and K. Kim, Phys. Rev. B **81**, 195107 (2010).
[37] C. Zhang, L. W. Harriger, Z. Yin, W. Lv, M. Wang, G. Tan, Y. Song, D. L. Abernathy, W. Tian, T. Egami, K. Haule, G. Kotliar, and P. C. Dai, Phys. Rev. Lett. **112**, 217202 (2014).
[38] Y. Li, Z. Yin, X. Wang, D. W. Tam, D. L. Abernathy, A. Podlesnyak, C. Zhang, M. Wang, L. Xing, C. Jin, K. Haule, G. Kotliar, T. A. Maier, and P. C. Dai, Phys. Rev. Lett. **116**, 247001 (2016).
[39] Y. Song, Z. Yamani, C. Cao, Y. Li, C. Zhang, J. S. Chen, Q. Huang, H. Wu, J. Tao, Y. Zhu, W. Tian, S. Chi, H. Cao, Y.-B. Huang, M. Dantz, T. Schmitt, R. Yu, A. H. Nevidomskyy, E. Morosan, Q. Si, and P. C. Dai, Nat. Commun. **7**, 13879 (2016).
[40] D. G. Quirinale, V. K. Anand, M. G. Kim, A. Pandey, A. Huq, P. W. Stephens, T. W. Heitmann, A. Kreyssig, R. J. McQueeney, D. C. Johnston, and A. I. Goldman, Phys. Rev. B **88**, 174420 (2013).
[41] Z. P. Yin, K. Haule, and G. Kotliar, Nat. Phys. **10**, 845 (2014).
[42] R. M. Moon, T. Riste, and W. C. Koehler, Phys. Rev. **181**, 920 (1969).
[43] O. J. Lipscombe, L. W. Harriger, P. G. Freeman, M. Enderle, C. Zhang, M. Wang, T. Egami, J. Hu, T. Xiang, M. R. Norman, and P. C. Dai, Phys. Rev. B **82**, 064515 (2010).
[44] P. Steffens, C. H. Lee, N. Qureshi, K. Kihou, A. Iyo, H. Eisaki, and M. Braden, Phys. Rev. Lett. **110**, 137001 (2013).
[45] H. Q. Luo, M. Wang, C. Zhang, X. Lu, L.-P. Regnault, R. Zhang, S. Li, J. Hu, and P. C. Dai, Phys. Rev. Lett. **111**, 107006 (2013).
[46] F. Waßer, C. H. Lee, K. Kihou, P. Steffens, K. Schmalzl, N. Qureshi, and M. Braden, Sci. Rep. **7**, 10307 (2017).
[47] Y. Li, W. Wang, Y. Song, H. Man, X. Lu, F. Bourdarot, and P. C. Dai, Phys. Rev. B **96**, 020404(R) (2017).
[48] A. P. Mackenzie and Y. Maeno, Rev. Mod. Phys. **75**, 657 (2003).
[49] I. I. Mazin and D. J. Singh, Phys. Rev. Lett. **79**, 733 (1997).
[50] J. H. Zhang, R. Sknepnek, and J. Schmalian, Phys. Rev. B **82**, 134527 (2010).
[51] C. Zhang, M. Wang, H. Luo, M. Wang, M. Liu, J. Zhao, D. L. Abernathy, T. A. Maier, K. Marty, M. D. Lumsden, S. Chi, S. Chang, J. A. Rodriguez-Rivera, J. W. Lynn, T. Xiang, J. Hu, and P. C. Dai, Sci. Rep. **1**, 115 (2011).
[52] R. Zhang, W. Wang, T. A. Maier, M. Wang, M. B. Stone, S. Chi, B. Winn, and P. C. Dai, Phys. Rev. B **98**, 060502(R) (2018).

Supplementary Information: Coexistence of ferromagnetic and antiferromagnetic spin fluctuations in $SrCo_2As_2$

I. SAMPLES PREPARATION AND EXPERIMENTAL METHODS

I.1 Sample Growth

Single crystals of $SrCo_2As_2$ were grown from solution using self-flux method with the ratio Sr:Co:As = 1:5:5. The elements were placed in an aluminum oxide crucible and sealed in an evacuated quartz tube. After heating slowly below 830°C, the mixture was cooked at 1200°C for 20 hours and then slowly cooled down to 1050°C with the rate 3°C/h and then down to 800°C with 10°C/h. Single crystals were obtained by cleaning off the flux. The typical sizes of the crystals were 1-2 centimeters.

I.2 Neutron Scattering

Our time-of-flight (TOF) neutron scattering measurements were carried out at the wide Angular-Range Chopper Spectrometer (ARCS) at Spallation Neutron Source, Oak Ridge National Laboratory and at the MAPS chopper spectrometer at the Rutherford-Appleton Laboratory, UK. The polarized neutron scattering measurements were done at the HB-1 Polarized Triple-Axis spectrometer (PTAX) at High Flux Isotope Reactor (HFIR), Oak Ridge National Laboratory and at the IN20 triple-axis spectrometer at the Institut Laue-Langevin, Grenoble, France.

We define the momentum transfer $\mathbf{Q}$ in three-dimensional reciprocal space in $Å^{-1}$ as $\mathbf{Q} = H\mathbf{a}^* + K\mathbf{b}^* + L\mathbf{c}^*$, where H, K, and L are Miller indices and $\mathbf{a}^* = \hat{\mathbf{a}}2\pi/a$, $\mathbf{b}^* = \hat{\mathbf{b}}2\pi/b$, $\mathbf{c}^* = \hat{\mathbf{c}}2\pi/c$ with $a = b \approx 5.56$ Å , and $c = 11.71$ Å [1]. Although $SrCo_2As_2$ has tetragonal structure with no static AF or FM order, we use this notation to facilitate easy comparison with AF ordered $SrFe_2As_2$ [2]. Our single crystals were co-aligned in the $[H, 0, L]$ scattering plane with mosaic less than 3° as shown in Fig. S1. For TOF measurement, the incident beam with energies of $E_i = 20, 35, 80, 250, 450$ meV is parallel to the c-axis of the crystals. In polarized neutron scattering experiments, we used $E_f = 13.5$ meV with neutron spin flipping ratio of $R \approx 10$ on HB-1 and $E_f = 14.7$ meV with $R \approx 17$ on IN20. About 10 grams of single crystals were used on ARCS and 25 grams on MAPS. We measured the same samples of 15 grams on HB-1 and another 7 grams at IN20.

In polarized neutron scattering experiments, the neutron polarization directions x, y, and z are defined as along $\mathbf{Q}$, perpendicular to $\mathbf{Q}$ but in the scattering plane, and perpendicular to both $\mathbf{Q}$ and the scattering plane [Fig. 3 (a)]. We measured all three neutron spin-flip (SF) scattering cross sections σ_x^{SF}, σ_y^{SF}, and σ_z^{SF}. For paramagnetic scattering with finite nonmagnetic background, we expect magnetic scattering to be $SIG = \sigma_x^{SF} - (\sigma_y^{SF} + \sigma_z^{SF})/2$.

I.3 Angle-resolved Photoemission Spectroscopy (ARPES)

ARPES measurements were performed at the Dreamline beam line of the Shanghai Synchrotron Radiation Facility using a Scienta DA80 analyzer and at the beam line 13U of the National Synchrotron Radiation Laboratory (Hefei) equipped with a Scienta R4000 analyzer. The energy and angular resolutions were set to 15 meV and 0.2°, respectively. Samples were cleaved *in situ*, yielding flat mirror-like (001) surfaces. During the measurements, the temperature was kept at 20 K and the pressure was maintained better than 5×10^{-11} Torr.

I.4 DFT+DMFT Calculation

Fully charge self-consistent density functional theory combined with dynamical mean-field theory (DFT+DMFT) [3, 4] was used to compute the electronic structures and spin dynamics of $SrCo_2As_2$ in the paramagnetic phase. Linearized augmented plane wave method as implemented in WIEN2K [5] was used for the DFT part. We used the same Hubbard $U = 5.0$ eV and Hund's coupling $J = 0.8$ eV as in our previous work on iron pnictides and chalcogenides [6–8]. The DMFT impurity problem was solved using continuous time quantum Monte Carlo (CTQMC) method [9, 10]. The dynamical spin structure factor was calculated with two-particle vertex corrections by using the method described in details in Refs. [6–8]. We use the experimentally determined crystal structures with lattice constants $a_T = 3.9466 \approx 5.56/\sqrt{2}$ Å and $c = 11.773$ Å, and As/Co atomic position (0, 0, 0.3587)/(0.5, 0, 0.25) [1].

II. EXPERIMENTAL RESULTS

We have measured magnetic susceptibility of $SrCo_2As_2$ and found no evidence of superconductivity above 1.8 K. In Figure S2, we plotted constant-energy scans along several directions in reciprocal space. These data are from TOF neutron scattering measurements obtained on ARCS and MAPS. At $E = 8$ meV, there exist antiferromagnetic (AF) and ferromagnetic (FM) spin fluctuations at in-plane wave vectors $\mathbf{Q}_{\rm AF} = (1, 0)$ and $\mathbf{Q}_{\rm FM} = (0, 0)/(2, 0)$. The one-dimensional cuts of AF spin fluctuations along the transverse (cut 1) and longitudinal (cut 2) directions are shown in Figures S2(c) and S2(e), respectively. The data reveal clear spin fluctuation anisotropy. We did not observe FM spin fluctuations at low energies in TOF data due to the strong phonon background. However, the presence of FM fluctuations can be demonstrated by polarized neutron scattering experiments on IN20 and HB-1. With increasing energy, AF spin fluctuations quickly disperse along the longitudinal direction but do not change much along the transverse direction [Figs. 2(a), 2(c), 2(e), 2(g)]. At $E = 50$ meV, along the transverse direction, AF and FM spin fluctuations merge together to form a square network [Fig. S2(b)]. In Figure. S2(f), we show the one-dimensional cut along the diagonal direction (cut 4). The red solid curve is the corresponding background subtracted from the raw data. The background curve is smooth around $(2, 0)$ suggesting that the peak is not due to the artificial background subtraction, but inherent in the raw data.

We note that since we observed FM and AFM fluctuations by different neutron techniques. In order to compare the strength of FM and AFM fluctuations, we converted the polarized neutron scattering intensity into the absolute units by comparing the intensity of AFM fluctuations at 8 meV which are observed in both time-of-flight and polarized neutron scattering experiments. The results was shown in Fig.1(h) and the peak in FM fluctuations was derived from the polarized neutron data in Fig.3(e).

We made a series of constant-E cuts along the transverse direction at different energies. Assuming the peak broadening [Figs. S2(c) and S2(d)] is due to the spin wave dispersion, the momentum of spin fluctuations at a particular energy is roughly half of the peak width. Therefore, we can obtain the dispersion relationship between the energy and momentum of spin fluctuations and estimate the effective spin wave velocity. Figure S3 shows the dispersion relationship of spin fluctuations with energy as x-axis and momentum as y-axis along the transverse direction. We fit the data with a linear function and estimate that the spin wave velocity along the transverse direction is about 440 meV$\cdot$ Å.

Figure S4 summarizes our polarized neutron scattering measurements on HB-1 where we find FM spin fluctuations at low energies. Polarized neutron scattering technique can be used to distinguish spin fluctuations from other nonmagnetic scattering. Polarized neutron scattering experiments were carried out with neutron polarization direction parallel and perpendicular to wave vector $\mathbf{Q}$, where $\sigma_{||\mathbf{Q}} = \sigma_x^{SF}$ and $\sigma_{\perp\mathbf{Q}} = (\sigma_y^{SF} + \sigma_z^{SF})/2$. The magnetic signal is then proportional to $SIG = \sigma_{||\mathbf{Q}} - \sigma_{\perp\mathbf{Q}}$. Figures S4(a) and S4(b) are constant-$\mathbf{Q}$ scans of $\sigma_{||\mathbf{Q}}$, $\sigma_{\perp\mathbf{Q}}$, and the corresponding backgrounds at AF and FM wave vectors. Since $\sigma_{||\mathbf{Q}} \geq \sigma_{\perp\mathbf{Q}} \geq BKG$ is generally true, there must be pure spin fluctuations at the probed wave vectors. Figure. S4(c) and S4(d) are constant-E scans of the three spin-flip scattering cross sections along the $[H, H, 3]$ and $[0, 0, L]$ directions, implying that spin fluctuations at FM wave vectors are confined in $\mathbf{Q}$-space. The isotropic spin fluctuations seen in FM and AF spin fluctuations in $SrCo_2As_2$ suggest that SOC is not as strong as that of $BaFe_2As_2$ in the AF ordered state.

Figure S5 shows the total and orbital contributions of dynamic spin susceptibility of $SrCo_2As_2$ calculated by DFT+DMFT method. Apparently, the components from the $d_{x^2-y^2}$ and d_{z^2} orbitals dominate the spectral weight of the total dynamic spin susceptibility while the other three t_{2g} components (d_{xy}, d_{xz}, and d_{yz}) have limited contribution. This is different from the dynamic spin susceptibility in iron pnictides where the t_{2g} orbitals play significant roles in determine the magnetic instability of the system.

Figure S6 shows the ARPES measurements at $k_z = \pi$ ($E_{photon} = 32$ eV). The intensity plot in Fig. S6(b) is along the A-Z direction and can be compared with DFT+DMFT results in Fig. S6(a). The intensity at the Fermi level around A point in Fig. S6(b) is the residual spectral weight from the band bottom above the Fermi level. This suggests that the flat band (yellow band) in (a) is right above the Fermi level and will have a large impact to the low energy behavior of the system. Figure S6(c) is the integrated intensity in the area contained by the dashed square in (b). The peak at the Fermi level cut off by the Fermi-Dirac function is suggestive of the existence of the band bottom right above the Fermi level. According to the DFT+DMFT results in Fig. S6(a), this band bottom has the contribution from the $d_{x^2-y^2}$ and d_{z^2} orbitals. This is consistent with the orbital analysis in Fig. S5 where the total dynamic spin susceptibility is dominated by e_g orbitals.

Figure S7 are the band structures of $SrCo_2As_2$ and $SrFe_2As_2$ calculated by DFT+DMFT method with and without spin-orbit coupling (SOC). The band structure in $SrCo_2As_2$ can be obtained from rigid band shift of $SrFe_2As2$, confirming it is electron doped. By comparing the results with and without SOC, it is clear that the SOC has a strong

effect on the t_{2g} orbitals rather than on the e_g orbital which is nearby the Fermi level in $SrCo_2As_2$. However, small gap associated with the flat band might open due to the SOC and have effects on the transport properties, which needs further investigation.

Figure S8 shows the DFT+DMFT calculated spin dynamic susceptibility $\chi''(\mathbf{Q}, E)$ at $\mathbf{Q}_{\rm FM} = (0, 0)$ (FM) and $\mathbf{Q}_{\rm AF} = (1, 0)$ (AF) wave vectors, and can be compared with data in Fig. 1(h). We find that the relative positions of maximum of the FM and AF spin fluctuations are opposite in the calculation and experiment. While the system in the calculation is in the proximity to the FM instability, our neutron scattering experiments suggest that the low-energy (below 10 meV) AF spin fluctuations are still dominating the spin fluctuation spectra in $SrCo_2As_2$. In particular, the energy scales in the experimental results have larger renormalization factors than the calculated ones, implying that the electron correlation in $SrCo_2As_2$ might be underestimated in the calculations.

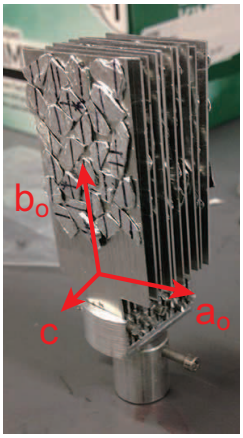

FIG. S1: Co-aligned $SrCo_2As_2$ single crystals in our neutron scattering experiments. The single crystals were coated with CYTOP and covered by Aluminum foil to avoid long-time exposure to the air and humidity. The samples are co-aligned in the $[H, 0, L]$ scattering plane.

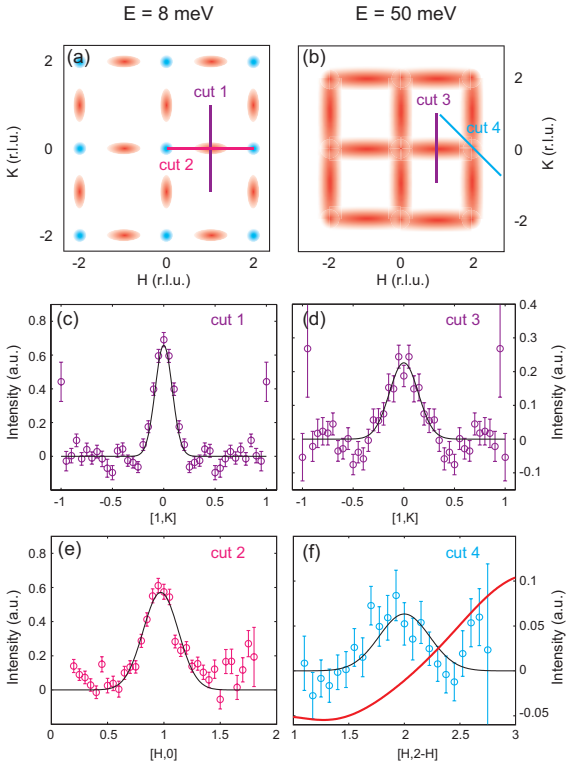

FIG. S2: (a) Schematics of spin fluctuations in the $[H, K]$ two-dimensional reciprocal space at $E = 8$ meV. Blue (red) areas represent FM (AF) spin fluctuations. (b) two-dimensional spin fluctuations at $E = 50$ meV. The FM and AF spin fluctuations merge together to form a squared ridge of scattering. (c-f) The corresponding one-dimensional cuts of the spin fluctuations as shown in (a) and (b). The red solid curve is the subtracted background. The background is smooth, suggesting that the bump-like feature in cut 4 is not due to background subtraction process.

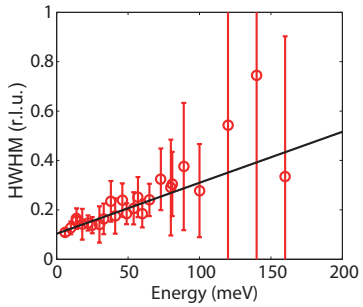

FIG. S3: (a) The half-width at half-maximum (HWHM) of AF spin fluctuations as a function of increasing energy along the transverse direction. The solid black line is the fitting result of a linear function. Assuming the peak broadening is due to the spin wave dispersion, the slope of this straight line is inversely proportional to the spin wave velocity estimated to be about 440 meV· Å.

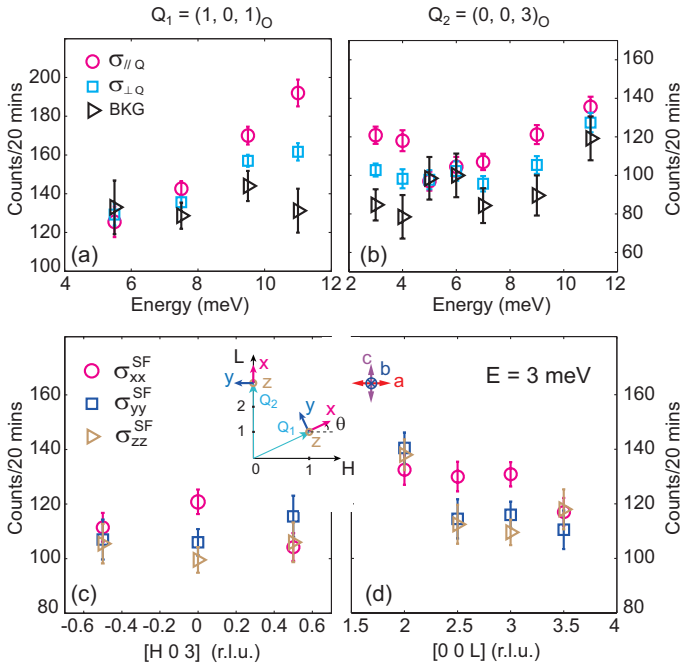

FIG. S4: Summary of polarized neutron scattering measured on HB-1. (a),(b) Constant-**Q** scans of AF spin fluctuations at $\mathbf{Q}_1 = (1, 0, 1)$, and FM spin fluctuations at $\mathbf{Q}_2 = (0, 0, 3)$. $\sigma_{||\mathbf{Q}}$ is equal to σ_x^{SF} and $\sigma_{\perp\mathbf{Q}}$ is the average of σ_y^{SF} and σ_z^{SF}, where x, y, z are neutron spin directions polarized along the **Q**, perpendicular to **Q** but in the scattering plane, and perpendicular to both **Q** and the scattering plane as shown in the inset of (c), (d) The three SF scattering cross section measured along the $[H, H, 3]$ and $[0, 0, L]$ directions at $E = 3$ meV.

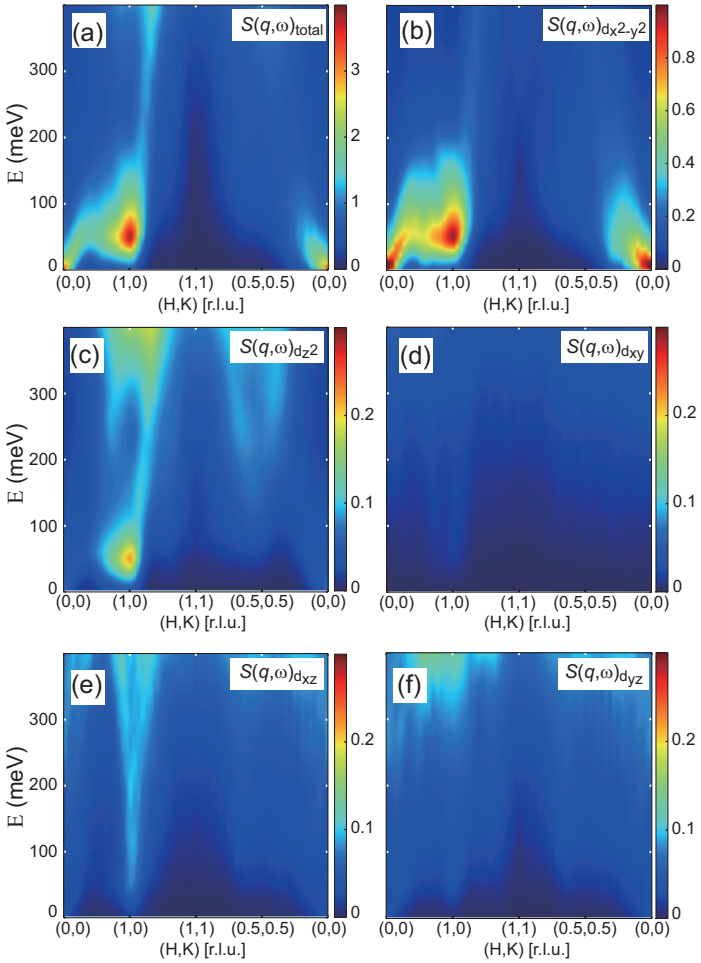

FIG. S5: The dynamic spin susceptibility calculated by DFT+DMFT method. The total spin susceptibility is shown in (a) and the contribution from the five intra-orbital channels are shown in (b-f). The main contribution of the total dynamic spin susceptibility is from $d_{x^2-y^2}$ and d_{z^2} orbitals while the three t_{2g} orbitals have limited contributions.

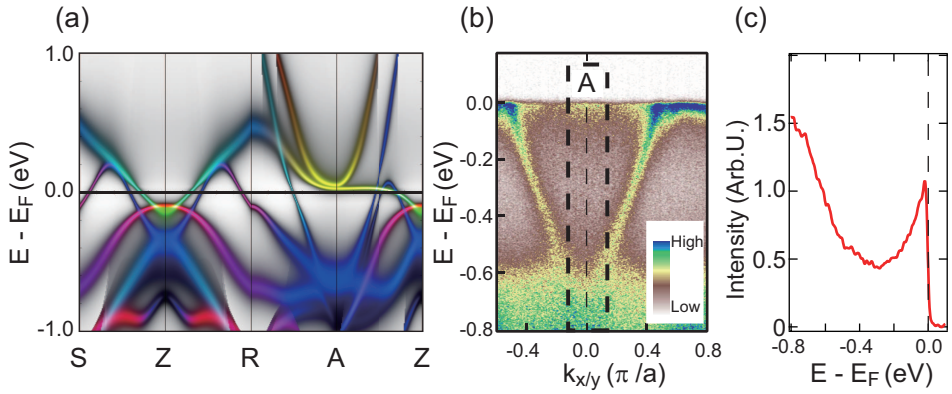

FIG. S6: (a) The electronic band structure calculated by DFT+DMFT method. Green (red) is the $d_{x^2-y^2}$ (d_{z^2}) and blue represents the t_{2g} orbitals. Yellow is the mixture of green ($d_{x^2-y^2}$) and red (d_{z^2}). (b) Intensity plots of band dispersion along the A-Z direction from ARPES measurements [Fig. 4(a)]. The intensity around A point at the Fermi level is the residual spectral weight from the flat band or the band bottom which has contributions from the $d_{x^2-y^2}$ and d_{z^2} orbitals. (c) The integrated intensity of the area contained by the dashed squared in (b).

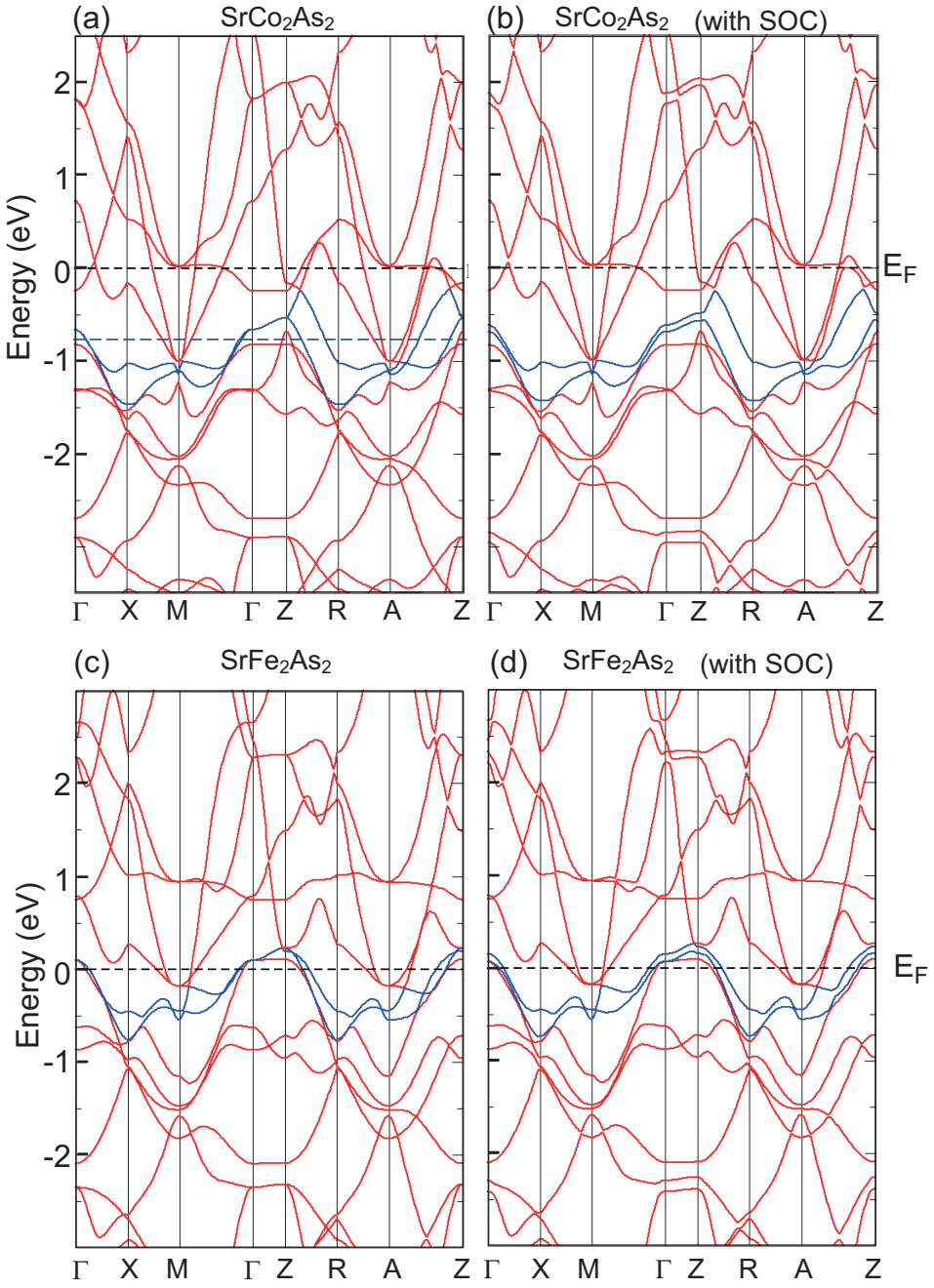

FIG. S7: Band structures of $SrCo_2As_2$ and $SrFe_2As_2$ calculated by DFT method without and with SOC, respectively. The energy corresponding to the Fermi level in $SrFe_2As_2$ was plotted as blue thick dash line in (a).

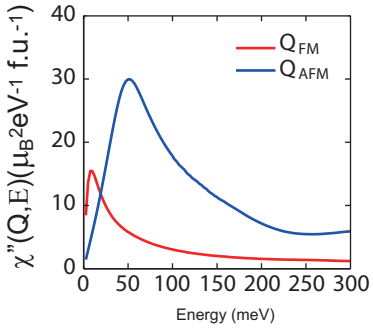

FIG. S8: Calculated spin dynamic susceptibility $\chi''(\mathbf{Q}, E)$ at $\mathbf{Q}_{\rm FM} = (0, 0)$ (FM) and $\mathbf{Q}_{\rm AF} = (1, 0)$ (AF) wave vectors.

[1] A. Pandey, D. G. Quirinale, W. Jayasekara, A. Sapkota, M. G. Kim, R. S. Dhaka, Y. Lee, T.W. Heitmann, P.W. Stephens, V. Ogloblichev, A. Kreyssig, R. J. McQueeney, A. I. Goldman, A. Kaminski, B. N. Harmon, Y. Furukawa, and D. C. Johnston, Phys. Rev. B **88**, 014526 (2013).

[2] D. C. Johnston, Adv. Phys. **59**, 803 (2010).

[3] G. Kotliar, S. Y. Savrasov, K. Haule, V. S. Oudovenko, O. Parcollet, and C. A. Marianetti, Rev. Mod. Phys. **78**, 865 (2006).

[4] K. Haule, C.-H. Yee, K. Kim Phys. Rev. B **81**, 195107 (2010).

[5] P. Blaha, K. Schwarz, G. Madsen, D. Kvasnicka, and J. Luitz, WIEN2K, An Augmented Plane Wave+Local Orbitals Program for Calculating Crystal Properties (Karlheinz Schwarz, Techn. Universität Wien, Austria, 2001).

[6] Z. P. Yin, K. Haule, and G. Kotliar, Nature Phys. **7**, 294 (2011).

[7] Z. P. Yin, K. Haule, and G. Kotliar, Nature Mater. **10**, 932 (2011).

[8] Z. P. Yin, K. Haule, and G. Kotliar, Nature Phys. **10**, 845 (2014).

[9] K. Haule, Phys. Rev. B **75**, 155113 (2007).

[10] P. Werner, A. Comanac, L. de' Medici, M. Troyer, and A. J. Millis, Phys. Rev. Lett **97**, 076405 (2006).